

# Scalable tensor network algorithm for quantum impurity problems

Zhijie Sun,<sup>1</sup> Ruofan Chen,<sup>2</sup> Zhenyu Li,<sup>1,\*</sup> and Chu Guo<sup>3,†</sup>

<sup>1</sup>*State Key Laboratory of Precision and Intelligent Chemistry,  
University of Science and Technology of China, Hefei 230026, China*

<sup>2</sup>*College of Physics and Electronic Engineering, and Center for Computational Sciences,  
Sichuan Normal University, Chengdu 610068, China*

<sup>3</sup>*Key Laboratory of Low-Dimensional Quantum Structures and Quantum Control of  
Ministry of Education, Department of Physics and Synergetic Innovation Center for  
Quantum Effects and Applications, Hunan Normal University, Changsha 410081, China*

The Grassmann time-evolving matrix product operator method has shown great potential as a general-purpose quantum impurity solver, as its numerical errors can be well-controlled and it is flexible to be applied on both the imaginary- and real-time axis. However, a major limitation of it is that its computational cost grows exponentially with the number of impurity flavors. In this work, we propose a multi-flavor extension of it to overcome this limitation. The key insight is that to calculate multi-time correlation functions on one or a few impurity flavors, one could integrate out the degrees of freedom of the rest flavors before hand, which could greatly simplify the calculation. The idea is particularly effective for quantum impurity problems with diagonal hybridization function, i.e., each impurity flavor is coupled to an independent bath, a setting which is commonly used in the field. We demonstrate the accuracy and scalability of our method for the imaginary time evolution of impurity problems with up to three impurity orbitals, i.e., 6 flavors, and benchmark our results against continuous-time quantum Monte Carlo calculations. Our method paves the way of scaling up tensor network algorithms to solve large-scale quantum impurity problems.

## I. INTRODUCTION

The dynamical mean field theory (DMFT) has been a major effective numerical tool to solve strongly correlated quantum many-body problems [1–3]. Instead of solving the original lattice problem, DMFT iteratively solves a quantum impurity problem (QIP) instead, in which an impurity is coupled to a noninteracting bath. In the past two decades, DMFT has been increasingly applied to solve realistic chemical or material problems beyond simple lattice models [4]. In these realistic situations, larger impurities have to be considered, and the scalability of the underlying quantum impurity solver basically determines the application range of DMFT.

The continuous-time quantum Monte Carlo (CTQMC) methods have been the golden standard for quantum impurity solvers [5–14]. They can yield numerically exact results, and are highly efficient on the imaginary-time axis, especially when the sign problem is not serious. However, real-time calculations remain a great challenge for CTQMC. A number of alternatives are also available, which complement CTQMC on the real-time axis or at zero temperature, including exact diagonalization [15–22], numerical renormalization group [23–35], hierarchical equation of motion [36–43], time-evolving matrix product state (MPS) [44–54]. Unlike CTQMC, these methods generally suffer from various sources of *uncontrolled numerical errors*, which could prohibit them from being used as general-purpose quantum impurity solvers.

The Grassmann time-evolving matrix product operator (GTEMPO) method, proposed by some of us, is a promising candidate as a general-purpose quantum impurity solver [55]. GTEMPO represents the integrand of the impurity path integral (PI), referred to as the augmented density tensor (ADT), as a Grassmann MPS (GMPS), in analogous to the time-evolving matrix product operator (TEMPO) method for bosonic impurity problems [56]. As the bath degrees of freedom are integrated out before hand via the Feynman-Vernon influence functional (IF) [57], GTEMPO is naturally free of the bath discretization error, similar to CTQMC. In fact, there are essentially only two sources of numerical errors in GTEMPO, one from discretization of the PI, the other from the MPS bond truncation. The first could be suppressed by using a finer time step size, while the second can be suppressed by using a larger bond dimension for MPS in principle. Meanwhile, as the core algorithms of GTEMPO only rely on the analytical expression of the IF, and that MPS algorithms are naturally free of the sign problem, GTEMPO can be flexibly applied on the imaginary-time axis [58], real-time axis (i.e., Keldysh contour) [59, 60], or even the L-shaped Kadanoff contour [61, 62].

However, a major drawback of GTEMPO is that its computational cost grows exponentially with the impurity size [58]. This could be understood from its formalism: in GTEMPO, the IF is similar to the partition function of a 1D long-range classical Hamiltonian on the temporal axis, if the impurity is small enough (e.g., a single flavor) to be treated as 0D. However, for a large number of impurity flavors, the impurity is no longer 0D, and the Hamiltonian becomes quasi-2D with a non-negligible spatial dimension. From the general experience

\* zyli@ustc.edu.cn

† guochu604b@gmail.com

of treating quasi-2D problems with MPS algorithms, the computational cost (or more concretely the MPS bond dimension) would grow exponentially with the size of the shorter side [63]. i.e, the number of flavors in our case.

In this work we propose a multi-flavor extension of the GTEMPO method to resolve this issue. As an impurity solver in DMFT, the central observables to calculate are the single-particle Green's functions which depends at most on two flavors. Therefore the degrees of freedom of the rest flavors can be integrated out before hand, similar to the treatment of the bath (although the flavor degrees of freedom can only be traced out numerically in general). Even though the full ADT may not be compressed, it is highly possible that the reduced ADT, which keeps only the information of the involved flavors, can be largely compressed without significant loss of accuracy. This idea is implemented in this work on top of GTEMPO, referred to as the *multi-flavor GTEMPO* method in the following. We note that a similar idea has been implemented in the bosonic case, based on TEMPO [64]. We apply this method to study imaginary-time evolution of QIPs with up to three orbitals (6 flavors), and benchmark our results against CTQMC. Our numerical results show that this method is indeed effective: under a commonly used semi-circular spectrum function of the bath, we observe that we can obtain highly accurate results (the error is of the same order with the chosen time step size) with bond dimensions 200 and 700 in the two-orbital and three-orbital cases respectively, which are far smaller than those from exponential growth. These results illustrate the power of the multi-flavor GTEMPO method to solve large-scale QIPs.

The paper is organized as follows. In Sec. II, we present the multi-flavor GTEMPO method. In Sec. III, we show our numerical results ranging from single-orbital to three-orbital QIPs, together with converged DMFT iterations, and benchmark them with CTQMC calculations. We summarize in Sec. IV.

## II. METHOD

### A. Model Hamiltonian

The Hamiltonian of the QIP can be generally written as

$$\hat{H} = \hat{H}_{\text{imp}} + \hat{H}_{\text{int}}, \quad (1)$$

where  $\hat{H}_{\text{imp}}$  denotes the impurity Hamiltonian, which can be generally written as

$$\hat{H}_{\text{imp}} = \sum_{p,q} t_{pq} \hat{a}_p^\dagger \hat{a}_q + \sum_{p,q,r,s} g_{pqrs} \hat{a}_p^\dagger \hat{a}_q^\dagger \hat{a}_r \hat{a}_s. \quad (2)$$

Here  $p, q, r, s$  are the fermion flavor labels that could contain both the spin and orbital indices,  $\hat{a}_p^\dagger$  and  $\hat{a}_p$  are the fermionic creation and annihilation operators of the  $p$ th impurity flavor,  $t_{pq}$  is the tunneling strength and  $g_{pqrs}$  is

the interaction strength.  $\hat{H}_{\text{int}}$  contains all the effects of the bath on the impurity. In this work, we consider  $\hat{H}_{\text{int}}$  in the following form:

$$\hat{H}_{\text{int}} = \sum_{p,k} \epsilon_{p,k} \hat{c}_{p,k}^\dagger \hat{c}_{p,k} + \sum_{p,k} v_{p,k} (\hat{a}_p^\dagger \hat{c}_{p,k} + \hat{c}_{p,k}^\dagger \hat{a}_p), \quad (3)$$

where  $\hat{c}_{p,k}^\dagger$  and  $\hat{c}_{p,k}$  are the fermionic creation and annihilation operators of the bath that is coupled to the  $p$ th impurity flavor,  $\epsilon_{p,k}$  is the band energy and  $v_{p,k}$  is the coupling strength between the impurity and bath. The first term on the right hand side of Eq.(3) is the free bath Hamiltonian and the second term is the coupling between the impurity and bath. We note that here we have restricted to diagonal coupling between impurity and bath, as each impurity flavor is coupled to its own bath in Eq.(3). We will further assume  $v_{p,k} = v_k$  for brevity (which does not lead to any significant simplification for GTEMPO). The effect of  $\hat{H}_{\text{int}}$  on the impurity dynamics is completely determined by the spectrum function, defined as  $J(\epsilon) = \sum_k v_k^2 \delta(\epsilon - \epsilon_k)$ . Throughout this work, we will consider a semi-circular spectrum function (which is also used, for example, in Refs. [47, 65])

$$J(\epsilon) = \frac{2}{\pi D} \sqrt{1 - (\epsilon/D)^2}, \quad (4)$$

in which we set  $D = 2$  and use it as the unit. We will focus on the imaginary-time evolution in this work, but we stress that our method can be straightforwardly applied to the Keldysh or Kadanoff contours as well.

### B. The multi-flavor GTEMPO method

The starting point of the GTEMPO method is the impurity path integral, which can be written as

$$Z = Z_{\text{bath}} \int \mathcal{D}[\bar{\mathbf{a}}\mathbf{a}] \mathcal{K}[\bar{\mathbf{a}}\mathbf{a}] \mathcal{I}[\bar{\mathbf{a}}\mathbf{a}] \quad (5)$$

where  $Z_{\text{bath}}$  is the partition function of the bath,  $\bar{\mathbf{a}}_p = \{\bar{a}_p(\tau)\}$ ,  $\mathbf{a}_p = \{a_p(\tau)\}$  are the Grassmann trajectories for the  $p$ th flavor over the whole imaginary-time interval  $[0, \beta]$  ( $\beta$  is the inverse temperature), and  $\bar{\mathbf{a}} = \{\bar{\mathbf{a}}_p, \bar{\mathbf{a}}_q, \dots\}$ ,  $\mathbf{a} = \{\mathbf{a}_p, \mathbf{a}_q, \dots\}$ . The measure  $\mathcal{D}[\bar{\mathbf{a}}\mathbf{a}]$  is

$$\mathcal{D}[\bar{\mathbf{a}}\mathbf{a}] = \prod_{p,\tau} d\bar{a}_p(\tau) da_p(\tau) e^{-\bar{a}_p(\tau) a_p(\tau)}. \quad (6)$$

$\mathcal{K}[\bar{\mathbf{a}}\mathbf{a}]$  denotes the contribution from the bare impurity dynamics determined by  $\hat{H}_{\text{imp}}$  only, which can be formally written as

$$\mathcal{K}[\bar{\mathbf{a}}\mathbf{a}] = e^{-\int_0^\beta d\tau \mathcal{H}_{\text{imp}}(\tau)}, \quad (7)$$

where  $\mathcal{H}_{\text{imp}}(\tau)$  is obtained from  $\hat{H}_{\text{imp}}$  by making the substitutions  $\hat{a}_p \rightarrow a_p(\tau)$ ,  $\hat{a}_p^\dagger \rightarrow \bar{a}_p(\tau)$ .  $\mathcal{I}[\bar{\mathbf{a}}\mathbf{a}]$  is the Feynman-Vernon IF that is determined by  $\hat{H}_{\text{int}}$  only. For

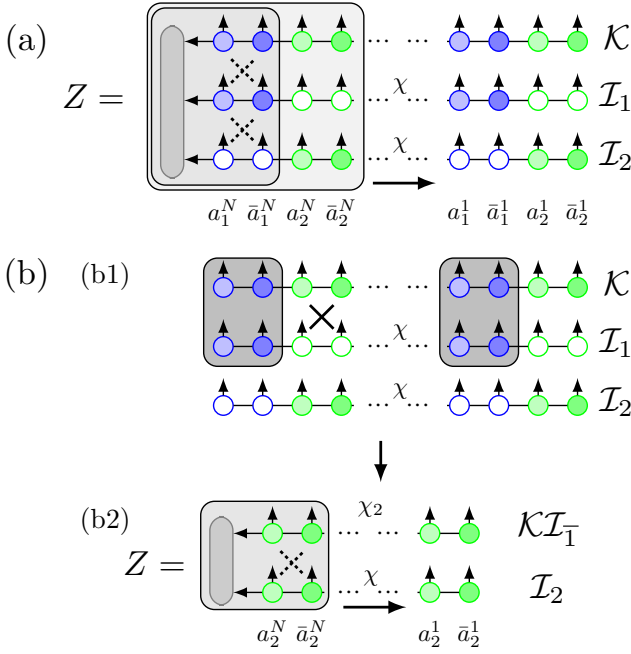


FIG. 1. (a) Schematic illustration of the zipup algorithm to calculate the partition function for an impurity problem with 2 flavors, where the quasi-2D tensor network is contracted (integrating out the pairs of conjugate Grassmann variables) from left to right and the augmented density tensor  $\mathcal{A}$  is calculated on the fly as indicated by the dashed  $\times$ . (b) The scheme used in the multi-flavor GTEMPO method to calculate the partition function based on the reduced ADT  $\mathcal{A}_2$  for the second flavor, in which one first calculate  $\mathcal{K}\mathcal{I}_1$  by multiplying  $\mathcal{K}$  and  $\mathcal{I}_1$  and integrating out the first flavor (b1), and then multiply  $\mathcal{K}\mathcal{I}_1$  and  $\mathcal{I}_2$  to obtain  $\mathcal{A}_2$  (b2). Again the second multiplication is only performed on the fly similar to (a). The empty circles in (b1) mean that these Grassmann variables do not exist in the corresponding GMPS, while the gray box means that the Grassmann variables inside it will be integrated out after multiplication.

diagonal hybridization function, the IF can be calculated as  $\mathcal{I}[\bar{a}a] = \prod_p \mathcal{I}_p[\bar{a}_p a_p]$  with  $\mathcal{I}_p[\bar{a}_p a_p]$  the IF of the  $p$ th flavor, which can be explicitly written as

$$\mathcal{I}_p[\bar{a}_p a_p] = e^{-\int_0^\beta d\tau' \int_0^\beta d\tau'' \bar{a}_p(\tau') \Delta(\tau', \tau'') a_p(\tau'')}. \quad (8)$$

The function  $\Delta(\tau', \tau'')$  in Eq.(8) is usually referred to as the hybridization function, which directly determines the IF, and can be calculated with the spectrum function and the free bath Matsubara Green's function [58]. The integrand in Eq.(5) defines the *augmented density tensor*, denoted as

$$\mathcal{A}[\bar{a}a] = \mathcal{K}[\bar{a}a] \prod_p \mathcal{I}_p[\bar{a}_p a_p], \quad (9)$$

which contains all the information of the multi-time impurity dynamics.

In GTEMPO, the continuous Grassmann trajectories  $\bar{a}_p, a_p$  are first discretized into  $N$  discrete Grassmann

variables (GVs) with equal-distant imaginary-time step size  $\delta\tau = \beta/N$ , then  $\mathcal{K}$  and  $\mathcal{I}_p$  are systematically constructed as GMPSs (one could see Ref. [58] for those details). The bond dimension of  $\mathcal{K}$  is generally a constant determined by the number of flavors, denoted as  $n$ , while the bond dimension of each  $\mathcal{I}_p$ , denoted as  $\chi$  in the following, will usually be larger than that of  $\mathcal{K}$ . With  $\mathcal{K}$  and  $\mathcal{I}_p$ , one could in principle multiply them together to obtain  $\mathcal{A}$  as a GMPS as in the definition of Eq.(9) (the multiplication of two GMPSs originates from the multiplication of two Grassmann tensors, which is analogous to the element-wise multiplication between two normal tensors [66]). Based on  $\mathcal{A}$ , one can easily compute any multi-time impurity correlation functions. For example, the Matsubara Green's function can be calculated as

$$G_{pq}(j\delta\tau) = \langle \hat{a}_p(j\delta\tau) \hat{a}_q^\dagger(0) \rangle = Z^{-1} \int \mathcal{D}[\bar{a}a] a_p^j \bar{a}_q^0 \mathcal{A}[\bar{a}a], \quad (10)$$

where  $\langle \hat{X} \rangle$  means the thermal average of operator  $\hat{X}$ . However, the bond dimension of  $\mathcal{A}$  will grow exponentially with  $n$  in general, or more concretely, as  $O(\chi^n)$  (and the computational cost will grow as  $O(\chi^{2n})$ ). A more efficient approach is to use the zipup algorithm, first proposed in Ref. [59], which directly contracts the quasi-2D tensor network made of  $\mathcal{K}$  and  $\mathcal{I}_p$  using a left to right sweep, during which  $\mathcal{A}$  is calculated on the fly (this strategy is similar to exactly contracting a 2D tensor network from the shorter side [67]). The zipup algorithm could reduce the computational cost down to  $O(\chi^n)$ , which is illustrated in Fig. 1(a). However, the cost is still exponential.

In the multi-flavor GTEMPO method, we resolve this exponential growth by realizing that to calculate  $G_{pq}(\tau)$ , one only needs the information of flavors  $p, q$ , and all the rest flavors can be integrated out before hand. We denote  $\mathcal{A}_{pq}[\bar{a}_{pq} a_{pq}]$  as the *reduced augmented density tensor* that only contains the  $p, q$  flavors, which can be calculated from  $\mathcal{A}[\bar{a}a]$  as:

$$\mathcal{A}_{pq}[\bar{a}_{pq} a_{pq}] = \int \mathcal{D}[\bar{a}_{\overline{pq}} a_{\overline{pq}}] \mathcal{A}[\bar{a}a]. \quad (11)$$

Here  $\overline{pq}$  means that all the flavors are included except  $p, q$ . With  $\mathcal{A}_{pq}$ , we can calculate  $G_{pq}(\tau)$  as

$$G_{pq}(\tau) = Z^{-1} \int \mathcal{D}[\bar{a}_{pq} a_{pq}] a_p^j \bar{a}_q^0 \mathcal{A}_{pq}[\bar{a}_{pq} a_{pq}]. \quad (12)$$

In the following, we will show our detailed numerical scheme to calculate the reduced ADT  $\mathcal{A}_{pq}$  (in fact, we will only calculate it on the fly as in the original zipup algorithm). Here we will focus on the case  $p = q = n$  and denote  $\mathcal{A}_{pq} = \mathcal{A}_n$ ,  $G_{pq} = G_n$ , but the procedure can be straightforwardly generalized to arbitrary  $p$  and  $q$ .

First, we multiply  $\mathcal{K}$  with  $\mathcal{I}_1$ , then we can integrate out the first flavor as the rest  $\mathcal{I}_p$ s contain no information of it, the result is denoted as  $\mathcal{K}\mathcal{I}_1[\bar{a}_1 a_1]$ :

$$\mathcal{K}\mathcal{I}_1[\bar{a}_1 a_1] = \int \mathcal{D}[\bar{a}_1 a_1] \mathcal{K}[\bar{a}a] \mathcal{I}_1[\bar{a}_1 a_1]. \quad (13)$$

After that, if there is still more than one flavor left, we multiply  $\mathcal{KI}_1$  with  $\mathcal{I}_2$  and integrate out the second flavor, and denote the result as  $\mathcal{KI}_{12}$ . Repeating this process, until that we have only  $\mathcal{I}_n$  left. In this stage, we can simply obtain  $\mathcal{A}_n$  by multiplying  $\mathcal{KI}_{1\dots n-1}$  and  $\mathcal{I}_n$ , however, we opt to keep them both and directly use them to calculate observables on the  $n$ th flavor using zipup algorithm. This scheme is schematically illustrated in Fig. 1(b) with the  $n = 2$  case. During this process, one needs to compress the intermediate GMPS (otherwise the bond dimension will still grow exponentially), i.e., the  $\mathcal{KI}_{1\dots j}$ s ( $1 \leq j < n$ ), for which we use another bond dimension  $\chi_2$ . For large impurities,  $\chi_2$  will generally be larger than  $\chi$  and determines the computational cost of the multi-flavor GTEMPO method.

To this end, we note that our scheme will be effective only if  $\chi_2 \ll O(\chi^n)$ . We argue that this behavior of  $\chi_2$  is expected. In fact, this scheme is similar to the boundary MPS method used to contract 2D tensor networks [68], but with a crucial difference: a partial integration is performed immediately after each GMPS multiplication, during which we *throw away* the information of the flavor being integrated out (the length of the resulting GMPS becomes shorter correspondingly). Therefore it is reasonable that the intermediate GMPSs can be significantly compressed without loss of accuracy. In comparison, it has been shown that if one directly contract the quasi-2D tensor network in Fig. 1(a) in full analogous to the boundary MPS algorithm without doing partial integration, then compression of the intermediate GMPSs will result in significant numerical errors [58].

In the next section, we will illustrate the effect of  $\chi_2$  on the numerical accuracy of  $G(\tau)$  with various examples ranging from one to three orbitals.

### III. NUMERICAL RESULTS

In our numerical examples, we will focus on calculating  $G_{pq}(\tau)$  with  $p = q = n$  and neglect the subscript. The CTQMC calculations in this work are performed using the TRIQS package [69, 70] with  $6.4 \times 10^9$  samples. As we consider  $\hat{H}_{\text{int}}$  that is symmetric for all the flavors,  $\mathcal{I}_p$  is the same for all flavors (which is not a significant simplification though, since the cost of calculating the reduced ADT dominates for large impurities), so can reuse the same  $\mathcal{I}_p$  across all our multi-flavor GTEMPO calculations for different number of flavors, as long as the bath parameters  $\beta$  and  $\delta\tau$  remain the same.

In GTEMPO, there are only two sources of numerical errors: (1) the time discretization error of the impurity PI, characterized by  $\delta\tau$ , and (2) the MPS bond truncation error, occurred in building each  $\mathcal{I}_p$  as a GMPS, characterized by  $\chi$ . In multi-flavor GTEMPO, there is an additional source of error, occurred in compressing the intermediate GMPSs  $\mathcal{KI}_{1\dots j}$ , characterized by  $\chi_2$  as indicated in Fig. 1(b). In the following, we will first analyze the errors of GTEMPO, against  $\chi$  and  $\delta\tau$  in

the single-flavor case in Sec. III A. Then we consider the single-orbital case in Sec. III B and the two- and three-orbital cases in Sec. III C, where we analyze the errors of our multi-flavor GTEMPO against  $\chi_2$ . Finally in Sec. III D, we demonstrate the effectiveness of our multi-flavor GTEMPO with two- and three-orbital converged DMFT iterations. We will use the mean error, defined as  $\sqrt{\sum_{i=1}^N |x_i - y_i|^2 / N}$  between two sets of results  $\mathbf{x}$  and  $\mathbf{y}$ , to characterize the error between GTEMPO or multi-flavor GTEMPO results and other calculations.

#### A. Toulouse model

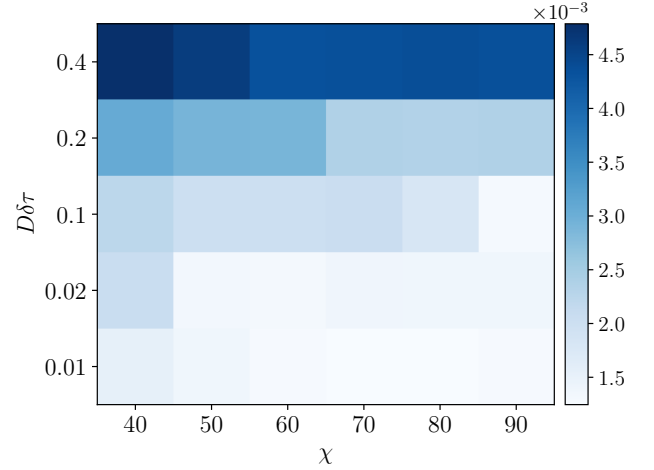


FIG. 2. Mean error of  $G(\tau)$  between GTEMPO and the analytical solution, as a function of  $\delta\tau$  and  $\chi$ , for the Toulouse model with  $\beta = 10$  and  $\epsilon_d = 1$ .

We first consider the single-flavor case with  $\hat{H}_{\text{imp}} = \epsilon_d \hat{a}^\dagger \hat{a}$ , referred to as the Toulouse model, which can be analytically solved [71]. We will fix  $\epsilon_d = 1$ . For this model there is only a single  $\mathcal{I}_1$  and there is no need to use the multi-flavor GTEMPO method. The purpose of this example is merely to find the proper values of the two hyperparameters  $\chi$  and  $\delta\tau$  that will be used in later multi-flavors calculations.

In Fig. 2, we show the mean error of  $G(\tau)$  between GTEMPO and the analytical solution as a function of  $\delta\tau$  and  $\chi$ , for the Toulouse model at  $\beta = 10$ . We observe that the accuracy systematically improves with smaller  $\delta\tau$  and larger  $\chi$ . In particular, with  $\delta\tau = 0.05$  and  $\chi = 60$  GTEMPO has already achieved an accuracy of  $2.0 \times 10^{-3}$ . Interestingly, even with a large  $\delta\tau = 0.2$  and a small  $\chi = 40$ , GTEMPO still achieves an accuracy of  $4.8 \times 10^{-3}$ , which illustrates the robustness and accuracy of it. In all the subsequent simulations, we will fix  $\delta\tau = 0.05$ .

In Fig. 3(a,b), we study the accuracy of GTEMPO results against different  $\chi$  for the Toulouse model at  $\beta = 10$



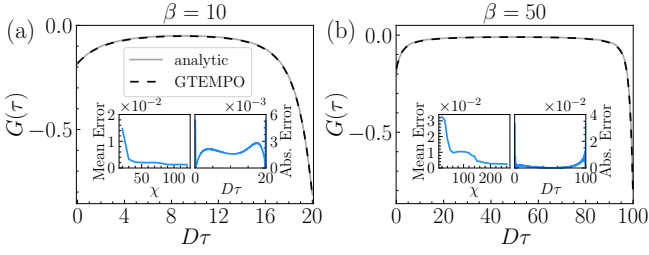


FIG. 3.  $G(\tau)$  for the Toulouse model at (a)  $\beta = 10$  and (b)  $\beta = 50$ . The gray solid lines and the black dashed lines represent the analytical solutions and the GTEMPO results respectively. The left inset in both panels shows the mean error between GTEMPO and the analytical solution as a function of  $\chi$ , while the right inset shows the absolute error of  $G(\tau)$  between GTEMPO and the analytical solution. We have used  $\chi = 60$  in the main panel (a) and its right inset, and used  $\chi = 200$  in the main panel (b) and its right inset.

and  $\beta = 50$ , respectively. We can see that the GTEMPO results generally agree very well with the analytical solutions. From the left insets, we can see that the mean error goes down monotonically with  $\chi$  in both cases. From the insets of both panels, we can see that the errors are generally larger at  $\beta = 50$  compared to  $\beta = 10$ , even though larger  $\chi$ s have been used, which indicates that GTEMPO has a larger computational cost at lower temperature.

### B. Single-orbital Anderson impurity model

Now we move on to the single-orbital case (2 flavors) where the multi-flavor GTEMPO method can be seriously tested. We consider the single-orbital Anderson impurity problem with

$$\hat{H}_{\text{imp}} = \epsilon_d \sum_{p=1}^2 \hat{n}_p + U \hat{n}_1 \hat{n}_2, \quad (14)$$

where  $\hat{n}_p = \hat{a}_p^\dagger \hat{a}_p$  is the electron density operator. We focus on the half-filling scenario with  $\epsilon_d = -U/2$ , which allows an easy justification of the results as  $G(0) = G(\beta) = -0.5$  is exactly satisfied in this scenario.

In Fig. 4, We consider four different parameter settings with different  $\beta$  and  $U$ , as shown in the titles of the four panels, to illustrate the accuracy of the multi-flavor GTEMPO in different cases. We have used  $\chi = 60$  for  $\beta = 10$  and  $\chi = 200$  for  $\beta = 50$ , and used  $\chi_2 = 60$  for all the simulations in the main panels. We can see from the main panels that the multi-flavor GTEMPO results generally agree very well with CTQMC, and the error is the largest at  $\beta = 50$  and  $U = 10$  which is expected. From the left insets of all the panels, we observe that the errors between multi-flavor GTEMPO and CTQMC decrease very quickly with  $\chi_2$  and well saturates with  $\chi_2 = 30$ . These results already illustrate the effectiveness of our method, since if we directly multiply  $\mathcal{K}$  and  $\mathcal{Z}_1$ , the bond dimension of the resulting GMPS will be

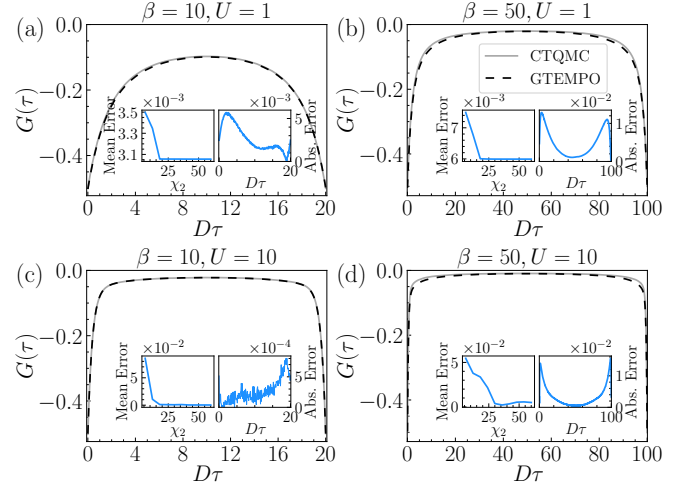


FIG. 4.  $G(\tau)$  as a function of  $\tau$  for the single-orbital Anderson impurity model with impurity Hamiltonian in Eq.(14), under different parameter settings as shown in the titles. The black dashed lines and the gray solid lines represent the multi-flavor GTEMPO results and the CTQMC results respectively. The left inset in all panels shows the mean error between multi-flavor GTEMPO and CTQMC as a function of  $\chi_2$ , the right inset shows the absolute error as a function of  $\tau$ . We have used  $\chi = 60$  for all the simulations in (a,c), and  $\chi = 200$  for all the simulations in (b,d). For all the main panels, and their right insets, we have used  $\chi_2 = 60$ .

$4\chi$  (the bond dimension of  $\mathcal{K}$  grows as  $2^n$ , which is 4 for this model), much larger than  $\chi_2$ . The right insets show the absolute errors between multi-flavor GTEMPO and CTQMC, which are on the order of  $10^{-3}$  for  $\beta = 10$ , and  $10^{-2}$  for  $\beta = 50$ .

### C. Multi-orbital quantum impurity models

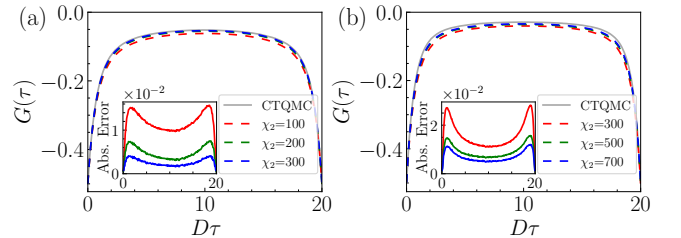


FIG. 5.  $G(\tau)$  for the two-orbital (a) and three-orbital (b) impurity problems with impurity Hamiltonian in Eq.(15). The gray solid lines in both panels represent the CTQMC results. The red, green and blue dashed lines represent multi-flavor GTEMPO results with  $\chi_2 = 100, 200, 300$  in (a), and represent multi-flavor GTEMPO results with  $\chi_2 = 300, 500, 700$  in (b). The insets show the absolute errors between multi-flavor GTEMPO and CTQMC results, where the colored solid line corresponds to multi-flavor GTEMPO result plotted in dashed line with the same color in the main panel.

In the next, we apply the multi-flavor GTEMPO method to study multi-orbital impurity problems, in which we will further fix  $\beta = 10$  and  $\chi = 60$  such that we can focus on analyzing the errors against  $\chi_2$ . We consider multi-orbital impurity Hamiltonian of the Slater-Kanamori type, given by [11]

$$\begin{aligned} \hat{H}_{\text{imp}} = & \epsilon_d \sum_p \hat{a}_p^\dagger \hat{a}_p + U \sum_x \hat{a}_{x,\uparrow}^\dagger \hat{a}_{x,\downarrow}^\dagger \hat{a}_{x,\downarrow} \hat{a}_{x,\uparrow} \\ & + (U - 2J) \sum_{x \neq y} \hat{a}_{x,\uparrow}^\dagger \hat{a}_{y,\downarrow}^\dagger \hat{a}_{y,\downarrow} \hat{a}_{x,\uparrow} \\ & + (U - 3J) \sum_{x > y, \sigma} \hat{a}_{x,\sigma}^\dagger \hat{a}_{y,\sigma}^\dagger \hat{a}_{y,\sigma} \hat{a}_{x,\sigma} \\ & - J \sum_{x \neq y} \left( \hat{a}_{x,\uparrow}^\dagger \hat{a}_{x,\downarrow}^\dagger \hat{a}_{y,\uparrow} \hat{a}_{y,\downarrow} + \hat{a}_{x,\uparrow}^\dagger \hat{a}_{y,\downarrow}^\dagger \hat{a}_{y,\uparrow} \hat{a}_{x,\downarrow} \right). \end{aligned} \quad (15)$$

Again we will focus on the half-filling scenario, with conditions

$$\epsilon_d = -(3U - 5J)/2; \quad (16)$$

$$\epsilon_d = -(2.5U - 5J), \quad (17)$$

for these two cases respectively [72, 73]. In our numerical simulations, we fix  $U = 4$  and  $J = 1$ , and  $\epsilon_d$  is set by the half-filling conditions.

In Fig 5(a,b), we plot  $G(\tau)$  as a function of  $\tau$  for the two- and three-orbital cases respectively, where the gray solid lines are CTQMC results, the red, green and blue dashed lines are multi-flavor GTEMPO results calculated with different  $\chi_2$ s. In the insets, we plot the absolute errors between multi-flavor GTEMPO and CTQMC. We can see that the absolute errors are of the order  $10^{-2}$  in both cases, and decrease monotonically with larger  $\chi_2$ . These results clearly illustrate the power of the multi-flavor GTEMPO method: we can already obtain very accurate results with absolute error around or smaller than  $10^{-2}$ , even though the  $\chi_2$  used in these two cases (which are 300 and 700 at most) are far smaller than those required by exponential growth, which are  $16 \times 60^3 \approx 3.5 \times 10^6$  and  $64 \times 60^5 \approx 5 \times 10^{10}$  respectively!

#### D. DMFT iterations on the Bethe lattice

Finally, we apply our multi-flavor GTEMPO as an impurity solver in DMFT, to solve the multi-orbital Slater-Kanamori mode [11] on the Bethe lattice. The hopping parameter of the Bethe lattice is chosen to be 1. To benchmark our results against CTQMC in a step-by-step fashion, we simply choose Eq.(4) as the initial spectral function for both solvers. We have performed 10 DMFT iterations in the two-orbital case with  $\chi_2 = 200$ , and 5 DMFT iterations in the three-orbital case with  $\chi_2 = 700$ . In both case the DMFT iterations have well converged, with mean errors between the last two iterations to be  $5.5 \times 10^{-5}$  and  $3.7 \times 10^{-4}$ . The results of

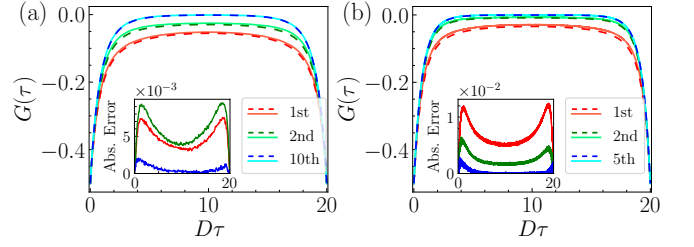


FIG. 6.  $G(\tau)$  at the 1st, 2nd, and final iterations in the DMFT calculation for the two-orbital (a) and three-orbital (b) DMFT iterations for the Slater-Kanamori model on the Bethe lattice. The dashed lines are the multi-flavor GTEMPO results at different iterations and the solid lines close to them are the corresponding CTQMC results. We have used  $\chi_2 = 200$  in (a) and  $\chi_2 = 700$  in (b). The insets show the absolute errors between multi-flavor GTEMPO and CTQMC results at different DMFT iterations.

the two cases are plotted in Fig. 6(a,b) respectively. In the insets we show the absolute errors between multi-flavor GTEMPO and CTQMC results. We can see that the absolute errors in both cases, and at different iterations, are all of the order  $10^{-2}$  or less, and interestingly, the errors in the last DMFT iteration is the smallest in both cases. These results thus illustrate the power of the multi-flavor GTEMPO method as a scalable quantum impurity solver.

#### IV. SUMMARY

In summary, we have proposed a multi-flavor Grassmann time-evolving matrix product operator method, which builds on top of the GTEMPO method and particularly targets at a large number of impurity flavors. The key insight is that to calculate observables on a single or a few flavors, one could integrate out the degrees of freedom of other flavors, resulting in a much smaller reduced augmented density tensor than the full ADT. In our numerical examples ranging from single-orbital to three-orbital quantum impurity problems, we have shown that in the multi-flavor GTEMPO method, the growth of the bond dimension of the involved GMPSSs is far slower than exponential which is required in vanilla GTEMPO. Under a commonly used semi-circular spectrum function of the bath, we observe that with bond dimensions 200 and 700 for the two-orbital and three-orbital cases, we can already obtain accurate Matsubara Green's functions whose absolute errors compared to CTQMC results are within the order of  $10^{-2}$ , we can also achieve converged DMFT iterations in which the multi-flavor GTEMPO results match the CTQMC results step by step.

In addition, we note that the multi-flavor GTEMPO method can be straightforwardly applied on the real-time axis, similar to the GTEMPO method. Moreover, it has been shown that the scaling of GTEMPO is better on the real-time axis than on the imaginary-time axis [58, 60],

since the anti-periodic boundary condition in the latter case would result in a larger bond dimension of the underlying GMPS. Due to the close relationship of the multi-flavor GTEMPO method to GTEMPO, we believe that it could be even more powerful for the (non-equilibrium) real-time evolution.

## ACKNOWLEDGMENTS

Z. L. is partially supported by NSFC (22393913) and the robotic AI-Scientist platform of Chinese Academy of Sciences R. C. acknowledges support from National Natural Science Foundation of China under Grant No. 12104328.

- 
- [1] A. Georges, G. Kotliar, W. Krauth, and M. J. Rozenberg, *Rev. Mod. Phys.* **68**, 13 (1996).
  - [2] A. Georges and G. Kotliar, *Phys. Rev. B* **45**, 6479 (1992).
  - [3] W. Metzner and D. Vollhardt, *Phys. Rev. Lett.* **62**, 324 (1989).
  - [4] G. Kotliar, S. Y. Savrasov, K. Haule, V. S. Oudovenko, O. Parcollet, and C. A. Marianetti, *Rev. Mod. Phys.* **78**, 865 (2006).
  - [5] A. N. Rubtsov and A. I. Lichtenstein, *J. Exp. Theor. Phys. Lett.* **80**, 61 (2004).
  - [6] A. N. Rubtsov, V. V. Savkin, and A. I. Lichtenstein, *Phys. Rev. B* **72**, 035122 (2005).
  - [7] P. Werner, A. Comanac, L. de' Medici, M. Troyer, and A. J. Millis, *Phys. Rev. Lett.* **97**, 076405 (2006).
  - [8] E. Gull, P. Werner, O. Parcollet, and M. Troyer, *EPL* **82**, 57003 (2008).
  - [9] C.-K. Chan, P. Werner, and A. J. Millis, *Phys. Rev. B* **80**, 235114 (2009).
  - [10] K. Haule, C.-H. Yee, and K. Kim, *Phys. Rev. B* **81**, 195107 (2010).
  - [11] E. Gull, A. J. Millis, A. I. Lichtenstein, A. N. Rubtsov, M. Troyer, and P. Werner, *Rev. Mod. Phys.* **83**, 349 (2011).
  - [12] L. Huang, T. O. Wehling, and P. Werner, *Phys. Rev. B* **89**, 245104 (2014).
  - [13] H. Lu and L. Huang, *Phys. Rev. B* **94**, 075132 (2016).
  - [14] C. Yue and P. Werner, *Phys. Rev. B* **104**, 184507 (2021).
  - [15] M. Caffarel and W. Krauth, *Phys. Rev. Lett.* **72**, 1545 (1994).
  - [16] E. Koch, G. Sangiovanni, and O. Gunnarsson, *Phys. Rev. B* **78**, 115102 (2008).
  - [17] M. Granath and H. U. R. Strand, *Phys. Rev. B* **86**, 115111 (2012).
  - [18] Y. Lu, M. Höppner, O. Gunnarsson, and M. W. Haverkort, *Phys. Rev. B* **90**, 085102 (2014).
  - [19] C. Mejuto-Zaera, L. Zepeda-Núñez, M. Lindsey, N. Tubman, B. Whaley, and L. Lin, *Phys. Rev. B* **101**, 035143 (2020).
  - [20] Y. Lu, X. Cao, P. Hansmann, and M. W. Haverkort, *Phys. Rev. B* **100**, 115134 (2019).
  - [21] R.-Q. He and Z.-Y. Lu, *Phys. Rev. B* **89**, 085108 (2014).
  - [22] R.-Q. He, J. Dai, and Z.-Y. Lu, *Phys. Rev. B* **91**, 155140 (2015).
  - [23] K. G. Wilson, *Rev. Mod. Phys.* **47**, 773 (1975).
  - [24] R. Bulla, *Phys. Rev. Lett.* **83**, 136 (1999).
  - [25] R. Bulla, T. A. Costi, and T. Pruschke, *Rev. Mod. Phys.* **80**, 395 (2008).
  - [26] F. B. Anders, *J. Phys. Condens. Matter* **20**, 195216 (2008).
  - [27] R. Žitko and T. Pruschke, *Phys. Rev. B* **79**, 085106 (2009).
  - [28] X. Deng, J. Mravlje, R. Žitko, M. Ferrero, G. Kotliar, and A. Georges, *Phys. Rev. Lett.* **110**, 086401 (2013).
  - [29] K. M. Stadler, Z. P. Yin, J. von Delft, G. Kotliar, and A. Weichselbaum, *Phys. Rev. Lett.* **115**, 136401 (2015).
  - [30] S.-S. B. Lee and A. Weichselbaum, *Phys. Rev. B* **94**, 235127 (2016).
  - [31] S.-S. B. Lee, J. von Delft, and A. Weichselbaum, *Phys. Rev. Lett.* **119**, 236402 (2017).
  - [32] P. S. Cornaglia, H. Ness, and D. R. Grempel, *Phys. Rev. Lett.* **93**, 147201 (2004).
  - [33] J. Paaske and K. Flensberg, *Phys. Rev. Lett.* **94**, 176801 (2005).
  - [34] P. S. Cornaglia, D. R. Grempel, and H. Ness, *Phys. Rev. B* **71**, 075320 (2005).
  - [35] M. A. Laakso, D. M. Kennes, S. G. Jakobs, and V. Meden, *New Journal of Physics* **16**, 023007 (2014).
  - [36] Y. Tanimura and R. Kubo, *J. Phys. Soc. Jpn.* **58**, 101 (1989).
  - [37] J. Jin, S. Welack, J. Luo, X.-Q. Li, P. Cui, R.-X. Xu, and Y. Yan, *J. Chem. Phys.* **126**, 134113 (2007).
  - [38] J. Jin, X. Zheng, and Y. Yan, *J. Chem. Phys.* **128**, 234703 (2008).
  - [39] Y. Yan, J. Jin, R.-X. Xu, and X. Zheng, *Front. Phys.* **11**, 110306 (2016).
  - [40] J. Cao, L. Ye, R. Xu, X. Zheng, and Y. Yan, *JUSTC* **53**, 0302 (2023).
  - [41] Q. Shi, Y. Xu, Y. Yan, and M. Xu, *The Journal of Chemical Physics* **148**, 174102 (2018), [https://pubs.aip.org/aip/jcp/article-pdf/doi/10.1063/1.5026753/15539991/174102\\_1.online.pdf](https://pubs.aip.org/aip/jcp/article-pdf/doi/10.1063/1.5026753/15539991/174102_1.online.pdf).
  - [42] Y. Yan, M. Xu, T. Li, and Q. Shi, *The Journal of Chemical Physics* **154**, 194104 (2021), [https://pubs.aip.org/aip/jcp/article-pdf/doi/10.1063/5.0050720/15977717/194104\\_1.online.pdf](https://pubs.aip.org/aip/jcp/article-pdf/doi/10.1063/5.0050720/15977717/194104_1.online.pdf).
  - [43] X. Dan, M. Xu, J. T. Stockburger, J. Ankerhold, and Q. Shi, *Phys. Rev. B* **107**, 195429 (2023).
  - [44] F. A. Wolf, I. P. McCulloch, O. Parcollet, and U. Schollwöck, *Phys. Rev. B* **90**, 115124 (2014).
  - [45] M. Ganahl, P. Thunström, F. Verstraete, K. Held, and H. G. Evertz, *Phys. Rev. B* **90**, 045144 (2014).
  - [46] M. Ganahl, M. Aichhorn, H. G. Evertz, P. Thunström, K. Held, and F. Verstraete, *Phys. Rev. B* **92**, 155132 (2015).
  - [47] F. A. Wolf, A. Go, I. P. McCulloch, A. J. Millis, and U. Schollwöck, *Phys. Rev. X* **5**, 041032 (2015).
  - [48] D. J. García, K. Hallberg, and M. J. Rozenberg, *Phys. Rev. Lett.* **93**, 246403 (2004).
  - [49] S. Nishimoto, F. Gebhard, and E. Jeckelmann, *Physica B Condens. Matter* **378-380**, 283 (2006).
  - [50] A. Weichselbaum, F. Verstraete, U. Schollwöck, J. I. Cirac, and J. von Delft, *Phys. Rev. B* **80**, 165117 (2009).

- [51] D. Bauernfeind, M. Zingl, R. Triebl, M. Aichhorn, and H. G. Evertz, [Phys. Rev. X \*\*7\*\*, 031013 \(2017\)](#).
- [52] D. Werner, J. Lotze, and E. Arrigoni, [Phys. Rev. B \*\*107\*\*, 075119 \(2023\)](#).
- [53] L. Kohn and G. E. Santoro, [Phys. Rev. B \*\*104\*\*, 014303 \(2021\)](#).
- [54] L. Kohn and G. E. Santoro, [J. Stat. Mech. Theory Exp. \*\*2022\*\*, 063102 \(2022\)](#).
- [55] X. Xu, C. Guo, and R. Chen, [J. Chem. Phys. \*\*161\*\*, 151001 \(2024\)](#).
- [56] A. Strathearn, P. Kirton, D. Kilda, J. Keeling, and B. W. Lovett, [Nat. Commun. \*\*9\*\*, 3322 \(2018\)](#).
- [57] R. P. Feynman and F. L. Vernon, [Ann. Phys. \*\*24\*\*, 118 \(1963\)](#).
- [58] R. Chen, X. Xu, and C. Guo, [New J. Phys. \*\*26\*\*, 013019 \(2024\)](#).
- [59] R. Chen, X. Xu, and C. Guo, [Phys. Rev. B \*\*109\*\*, 045140 \(2024\)](#).
- [60] R. Chen, X. Xu, and C. Guo, [Phys. Rev. B \*\*109\*\*, 165113 \(2024\)](#).
- [61] R. Chen and C. Guo, [Phys. Rev. B \*\*110\*\*, 165114 \(2024\)](#).
- [62] Z. Sun, R. Chen, Z. Li, and C. Guo, [arXiv:2412.04702 \(2024\)](#).
- [63] U. Schollwöck, [Ann. Phys. \*\*326\*\*, 96 \(2011\)](#).
- [64] G. E. Fux, D. Kilda, B. W. Lovett, and J. Keeling, [Phys. Rev. Res. \*\*5\*\*, 033078 \(2023\)](#).
- [65] F. A. Wolf, I. P. McCulloch, and U. Schollwöck, [Phys. Rev. B \*\*90\*\*, 235131 \(2014\)](#).
- [66] C. Guo and R. Chen, [SciPost Phys. Core \*\*7\*\*, 063 \(2024\)](#).
- [67] C. Guo, Y. Liu, M. Xiong, S. Xue, X. Fu, A. Huang, X. Qiang, P. Xu, J. Liu, S. Zheng, H.-L. Huang, M. Deng, D. Poletti, W.-S. Bao, and J. Wu, [Phys. Rev. Lett. \*\*123\*\*, 190501 \(2019\)](#).
- [68] F. Verstraete, J. J. García-Ripoll, and J. I. Cirac, [Phys. Rev. Lett. \*\*93\*\*, 207204 \(2004\)](#).
- [69] O. Parcollet, M. Ferrero, T. Ayrál, H. Hafermann, I. Krivenko, L. Messio, and P. Seth, [Comput. Phys. Commun. \*\*196\*\*, 398 \(2015\)](#).
- [70] P. Seth, I. Krivenko, M. Ferrero, and O. Parcollet, [Comput. Phys. Commun. \*\*200\*\*, 274 \(2016\)](#).
- [71] G. D. Mahan, *Many-Particle Physics* (Springer; 3rd edition, 2000).
- [72] A. Sherman, [Phys. Scr. \*\*95\*\*, 095804 \(2020\)](#).
- [73] P. Werner, E. Gull, and A. J. Millis, [Phys. Rev. B \*\*79\*\*, 115119 \(2009\)](#).